CHAPTER

12 IR spectroscopy and imaging using polarized light with QCLs: instrumentation and applications

Ruo-Jing Ho[1,2], Yamuna Phal[1,3], Laurin Lux[1] and Rohit Bhargava[1,2,3,4,5]

[1]*Beckman Institute for Advanced Science and Technology, Urbana, IL, United States;* [2]*Department of Bioengineering, Urbana, IL, United States;* [3]*Department of Electrical and Computer Engineering, Urbana, IL, United States;* [4]*Departments of Chemistry, Chemical and Biomolecular Engineering, Mechanical Science and Engineering, Urbana, IL, United States;* [5]*Cancer Center at Illinois, University of Illinois at Urbana-Champaign, Urbana, IL, United States*

1. Introduction

Infrared (IR) spectroscopy and microspectroscopy are well-established techniques in the field of analytical chemistry. They provide the unique capability of combining qualitative and quantitative chemical information in a nondestructive way. With applications spanning from chemical sensing and polymer analysis [1,2] to digital pathology [3,4], IR spectroscopy and imaging have revolutionized a myriad of fields. Over decades, Fourier transform (FT) spectrometers that relied on the combination of thermal light sources with interferometry techniques were considered the gold standard in IR spectroscopy. This was largely due to the multiplexing (Fellgett's advantage) and throughput (Jacquinot's advantage) advantages of FT-IR spectroscopy [5]. The benefits of high brightness light sources [6] were discovered early by the combination of synchrotron radiation with IR microspectroscopy. Although the results were clearly promising, the limited accessibility of synchrotron sources was an unrivaled challenge [7–9].

Ingenious method of using array detectors combined with interferometry [10–13] provided advancements in speed and sensitivity for imaging. This modality demonstrated numerous applications such as the study of reaction kinetics [14,15] in time-resolved [16] or multiplexed configurations [17,18]. Recent years have seen improvements in instrument design and technology [19–21] with enhanced image quality using attenuated total reflection [12,22] or synchrotron-focal plane arrays [23]. High-definition IR imaging systems with high dynamic range and sensitivity have now become routine.

Among other advancements, the fabrication of laser sources known as quantum cascade lasers (QCLs) emitting in the mid-infrared (MIR) region [24–26] has led to a new era of IR spectroscopy and imaging [27]. Higher light intensities of the laser allow measurements in highly absorbing media such as H_2O. Consequently, the introduction of QCLs provided magnitudes of improvement in both speed and signal-to noise ratio (SNR). Especially for imaging applications, it is often superfluous to obtain data points over the whole spectral range. Instead of acquiring the entire spectral dataset, the discrete

Molecular and Laser Spectroscopy. https://doi.org/10.1016/B978-0-323-91249-5.00012-0

frequency infrared (DFIR) technique recognizes and exploits the redundancy in the high-dimensional spectral data and provides significant speed-ups in imaging time. The acquisition process can thereby be accelerated from a couple of days to a couple of minutes. Besides the improvement of existing methods, the application of QCL light sources enabled hybrid measurement techniques with mechanical scanning probes, atomic force microscopy-IR (AFM-IR) spectroscopic imaging [28–30], and IR-optical hybrid (IR-OH) microscopy [31] that take advantage of secondary effects that are caused by absorption. Moreover, the inherent characteristics of laser radiation paved the way for integration of polarization [32,33] and vibrational circular dichroism (VCD) capabilities [34–36] along with standard measurements. Both hardware and software innovations have also paved the way for improved resolution and detection limits in IR [37–39].

The transition from FT-IR to DFIR might seem to stem from a mere difference in the light source—but it is not the case. Specifically, the change leads to disparate instrumental designs. First and foremost, QCLs emit coherent light with narrow linewidth, while the globar is a broadband emitter with wide spectral bandwidth. In the context of spectral resolution, FT-IR technique solely depends on the length of the interference signal, which is a competing factor with the scan speed. With QCL-based systems, the laser configuration plays a major role in the system performance. Compared to FT-IR modality, which is based on the decoupling of spectral bands from the interference signal using FT, QCLs can tune to the individual wavenumbers directly, one band at a time. These fundamental distinctions between FT-IR and DFIR modalities necessitate rethinking of the imaging system at various degrees. The high throughput and laser pulsing characteristics of QCLs result in radical alterations in data acquisition as well. For instance, new inspections are needed to choose a suitable detector to match the response time, detectivity, and dynamic range and operation modes of the laser. Moreover, digitization speed and resolution are required to adapt the laser's emission behavior. With the pulsing property, QCLs permit versatile SNR enhancement techniques beyond simple apodization methods used in FT-IR. The knowledge presented here is especially vital for current or prospective developers of IR spectroscopy technology to exploit QCLs. Although QCL-based systems are still limited in their commercial availability, they already have a significant influence in the field of IR spectroscopy. It is foreseeable that both FT-IR and QCL-based spectroscopy will play an important part in the future of IR spectroscopy. Considering that, it is worthwhile to take a closer look into the field of QCL-based imaging and spectroscopy.

In Section 3, we elaborate instrumentation details of QCL-based spectrometers, specifically focusing on lasers, detectors, back-end control, and data acquisition systems. Additionally, modulation techniques can provide novel alternatives to enhance SNR while enabling increased measurement sensitivity. In this regard, we also describe different modulating devices. In Section 3.4, we talk about specific characteristics of the systems that are closely related to the usage of QCLs instead of conventional light sources. Finally, Section 5 provides an overview of crucial applications where QCL-based systems have outperformed conventional systems.

2. Theoretical background

The state of polarization is an important aspect for any laser and is identified as the direction in which the electric field is vibrating—in a direction orthogonal to the beam axis. Theoretically, the polarization state of an optical beam can be described by the Stokes vector [40].

$$\mathbf{S} = \begin{Bmatrix} I \\ Q \\ U \\ V \end{Bmatrix} = \begin{Bmatrix} I_T \\ I_{0^\circ} - I_{90^\circ} \\ I_{45^\circ} - I_{135^\circ} \\ I_R - I_L \end{Bmatrix} \tag{12.1}$$

where I is the total intensity and sum of all the orthogonal polarizations, Q and U are the differences in the linear polarization components, and V is the differential circular polarization component and is equal to the difference between right-circularly polarized (RCP) and left-circularly polarized (LCP) components [34]. Although most QCLs are linearly polarized, they can have other residual polarization contributions. Janassek et al. [41] describe how it is possible to experimentally determine the Stokes parameters for a QCL. Their results are based on an experimental setup that combines a polarizer and a quarter-wave plate to measure the transmitted light intensity at different angles of the quarter-wave plate. Based on these experiments, it was found that QCLs also emit a nonnegligible amount of circularly polarized light. When the output light intensity of the laser is perfectly linearly polarized, it follows the equation:

$$I = I_0 \cos^2 \theta \tag{12.2}$$

where I is the light intensity after a polarizer, I_0 is the incident light intensity, and θ describes the polarization angle. Fig. 12.1 describes this relation empirically for different wavenumbers of a QCL consisting of four different laser chips. It can be easily seen that deviations occur from the ideal fit. These deviations can be attributed to the nonlinear polarized nature of the QCL and other alignment errors. Although this procedure alone does not allow for a full characterization of the Stoke parameters, it provides an insight into the polarization state of the emitted beam. Apparently, it is not possible to achieve a perfect polarization setting over the whole wavenumber region, nevertheless the angle deviations and the resulting transmission losses are only minimal as depicted in Fig. 12.3B and C. Inconsistent changes of the polarization characteristics occur at the transition between laser chips, indicated by the dashed red lines in Fig. 12.3B–D. The chip transition also affects the output intensity (amplitude) and can be observed in the emission profile of a representative QCL system as displayed in Fig. 12.3D.

Quantification of polarization properties can not only characterize the light source but also the optical components for system calibration and structural mapping of nonabsorbing samples. For example, following the Stokes vector formalism, degree of linear (DLP) and circular (DCP) polarization were demonstrated to calibrate polarimeters [42] and imaging of semiconductors' nanostructures [43]. The definitions shown below may vary for different light source polarization properties and research focus.

$$\mathrm{DLP} = \frac{\sqrt{Q^2 + U^2}}{I} \tag{12.3}$$

$$\mathrm{DCP} = \frac{V}{I} \tag{12.4}$$

Dichroism and birefringence are two main material properties describing the interaction of polarized illumination with any material. Specifically, dichroism occurs when the light absorption is

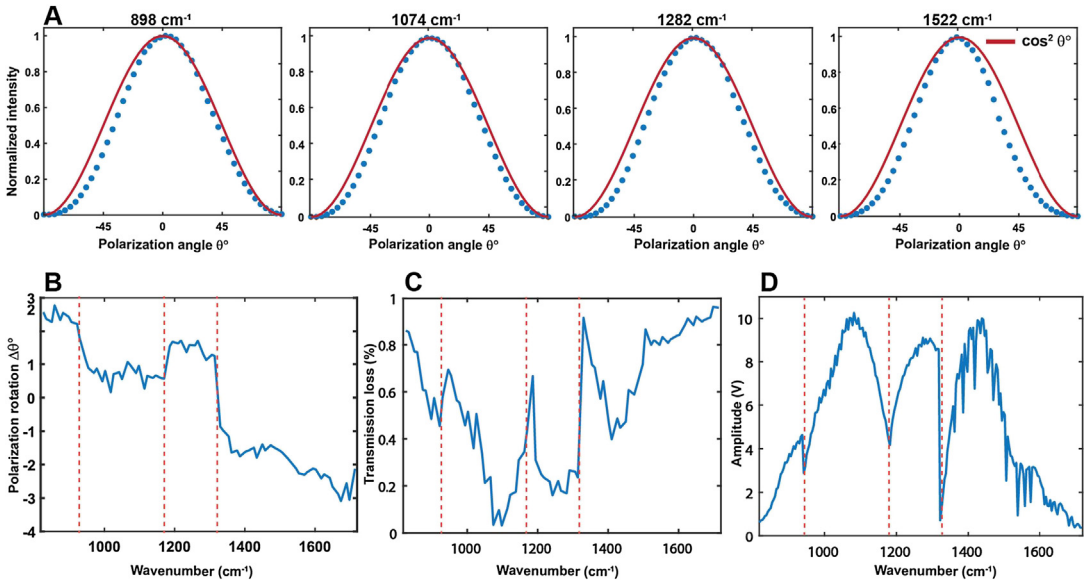

FIGURE 12.1

Laser polarization characterization. (A) Intensity variation with polarization angle of the four center wavenumbers of a representative laser. Theoretical $\cos^2(\theta^\circ)$ fit is shown with a solid red line. (B) The polarization rotation angle $\Delta\theta^\circ$ spectral variation calculated by $\cos^2(\theta^\circ - \Delta\theta^\circ)$ fitting. (C) The transmission loss from zero-degree polarizer ($\theta = 0^\circ$) for the entire wavenumber range. (D) The laser power spectrum depicted with the detected signal amplitude. Laser emission transitions are illustrated with the *dash lines* in (B–D).

polarization-dependent, and birefringence manifests the polarization-dependent refractive behavior. The Kramers–Kronig relations between dichroism and birefringence suggest the two properties stem from the polarization dependency of the real (n', birefringence) and imaginary (n'', dichroism) part of the refractive index (n), which can be expressed as, $n(S) = n'(S) + in''(S)$, where S denotes the polarization state of the incident light.

Therefore, the propagated light through the material becomes, $E(r, t) = E_0 e^{i(k_0 \cdot n(S) r - \omega t)}$, where E_0 denotes the amplitude, k_0 the wave vector in the vacuum, and $\boldsymbol{\omega}$ the oscillation frequency. Above equations show that $n''(S)$ leads to light attenuation. Dichroism properties have been utilized to reveal structural details of absorbing samples and chirality. For example, linear dichroic (*LD*) gauges optical anisotropy and can identify orientations of macromolecular structures [32], which is defined as $\mathrm{LD} = A_{||} - A_{\perp}$, where $A_{||}$ and $A_{\perp}$ denote the absorbance upon incident illuminations with polarization direction parallel and perpendicular to the specimen's structural orientations, respectively. On the other hand, circular dichroism (CD) measures the absorption difference for RCP (A_{RCP}) and LCP (A_{LCP}) light, $CD = A_{\mathrm{RCP}} - A_{\mathrm{LCP}}$. Using IR to measure CD is known as VCD because it originates from the induced rotational strength difference. VCD is widely observed in biological and pharmaceutical molecules and can be utilized for monitoring conformational changes such as protein aggregations, which are related to many pathological alterations. One of the VCD applications is demonstrated in Section 5.4.

3. Instrumentation

Intrinsically, DFIR instrument design differs significantly from FT-IR design. This fundamental difference requires rethinking of not only the back-end software implementation such as laser tuning and signal acquisition but also postprocessing steps such as noise reduction strategies. Together, it also underlines the significance of laser characterization, particularly for highly sensitive measurements (Section 3.4). A typical QCL spectrometer consists of a laser source, optics, a detector, and a back-end data acquisition system that is strongly application-specific. In this section, we first introduce the concept of laser tuning followed by implementation examples. Secondly, we describe the common IR detection modules and discuss the design considerations. Then, several data acquisition schemes are presented with discussion of the trade-offs between laser tuning modes, noise reduction, and implementation methods. Being intrinsically polarized, there is a recent trend toward using QCL spectrometers in combination with external modulation techniques to investigate sample structures that are typically not revealed by standard absorption measurements. Toward the end, we describe the principles of routinely used modulating devices such as photoelastic modulators (PEMs) and optical choppers along with the prototypical configurations. Over all, the goal of this section is to provide a setup guideline for a QCL spectroscopic system from both hardware and software perspectives to give readers a glimpse of the emerging instrumentation design trend.

3.1 Laser

QCLs are semiconductor lasers with heterostructures that allow cascaded intersubband stimulated emissions [24]. Within these heterostructures, the band gaps are tailored such that the emitted photons can tunnel through the adjacent layers and induce a series of subsequent optical emissions. Since the emission wavelength can be engineered by changing layer thickness and material compositions, QCLs provide a large tunable spectral range. Based on the resonator configurations, QCLs are categorized into Fabry−Perot (FP), distributed feedback (DFB), and external cavity (EC). FP-QCLs are based on the concept of resonators and consist of two high-reflectivity parallel mirrors acting as a wavelength filter wherein light experiences multiple reflections. The transmitted beam is typically multimode, and the reflectivities of the mirrors not only affect the energy loss but also the filtering bandwidth. With the simplest designs, FP-QCLs allow a relatively straight-forward approach for tuning to the desired wavelength. However, they are not suitable for applications requiring single-mode emissions. Alternatively, DFB is an extended configuration of FP designs, where a distributed Bragg reflector laser is used to fine-tune the optical emission using a Bragg scattering structure whose periodic refractive index can amplify the first-order diffraction and abase higher-order modes. This enables single-mode selection and a narrow linewidth that is suitable for gas-phase spectroscopic measurements. However, the complementary grating and refractive index configuration also restrict the tuning range. On the other hand, EC-QCLs have a FP resonator with an external grating for laser tuning, which greatly expands the available spectral range. As such, EC-QCLs allow fast and wide-range laser-tuning, which is a critical design requirement for spectroscopic imaging development.

3.2 Detectors

Conventional IR detectors can be categorized into thermal detectors and photon (quantum) detectors. The former detect a temperature change and convert the thermal energy into an electric signal output. The later are based on the photoelectric effect and measure the generated charge carriers upon an

incident illumination. Since the temperature change is only associated with the incident energy, thermal detectors have a uniform response across a wide spectral range. Thus, defining responsivity as the ratio of the output signal voltage to the input light power, thermal detectors demonstrate a flat spectral responsivity. On the contrary, responsivity of photon detectors is wavelength-dependent. Since the photoelectric effect is based on the optical excitation processes occurring in the material, the detectable wavelengths are restricted to the ones that match material's energy levels or engineered energy band gaps. Hence, their bandwidths are typically smaller than those of thermal detectors. In this case, since more photons are required to generate the same illumination power with higher wavelengths, responsivity is proportional to wavelength until the cut-off wavelength (material dependent) drops toward higher wavelengths [44].

In addition to spectral response, the noise characteristics and detection speed vary as well. Thermal detectors are mainly subjective to thermal noise. Furthermore, the response coefficients including thermal conductance (bolometers), pyroelectric coefficients (pyroelectric detectors), and Seebeck coefficients (thermopiles) are all temperature-dependent. Additionally, the speed is limited by the intrinsic thermal time constant, which is usually above 1 ms (around 10 Hz). In general, photon detectors exhibit faster response and better SNR than thermal detectors under cryogenic cooling conditions. Upon illumination, incident photons initiate the optical excitation and propagate the energy within the semiconductor material. While having a smaller spectral bandwidth, the detection mechanism is more efficient in terms of the response time constant, which typically lies below 1 μs. In addition, quantum efficiency describes the conversion ratio between the incident photons and generated carriers, and a higher value can be achieved with optimized fabrications such as surface coatings and vacuum conditions. Photoconductive (PC) and photovoltaic (PV) detectors are the two major types of photon detectors. PV detectors measure the current that results from the photonic absorption across a p−n junction, and PC detectors measure electricity conductivity changes due to the increase of the free carriers. Depending on the material's resistance, either a bias voltage or current is applied to the PC detector to enhance the measurement sensitivity. While the electrical bias results in a higher gain, photon recombination may happen at the electrode contacts. In comparison, p−n junctions of PV detectors separate the electron-hold pairs and hinder the recombination noise. Therefore, PV detectors ideally have $\sqrt{2}$ times lower noise level than PC detectors. Furthermore, as the responsivity of PC detectors relies on carriers' lifetime, the electric bandwidth is limited compared to the PV detectors.

Normalized detectivity, or D^* (D-star), is usually used to evaluate a detector's performance. Detectivity is defined as the reciprocal of noise equivalent power (NEP), which is the incident power that generates output signal with the same level as the detector's noise level. A small NEP value suggests low detector noise and more capability in detecting weak signals. While thermal detectors have a uniform spectral response and are utilized for FT-IR spectroscopy, they have a longer response time making them impractical for imaging applications. QCL-based microscopes in comparison can be used in combination with bolometer detectors, due to the strong illumination over a wide field-of-view [3]. Fig. 12.2 shows detectivity comparison of three commercially available PV detectors, which are photovoltaic multiple junction detectors (PVMI), standard PV detectors with two different materials—mercury cadmium telluride (MCT) and InSb. MCT and InSb detectors exhibit disparate spectral coverage based on the intrinsic material properties. While using the same active element material, PVMI detectors demonstrate a flat spectral response curve with enhanced detectivity and an expanded spectral coverage compared to conventional PV detectors. Immersion technology further improves the D^* by almost $\sim$11-fold [45].

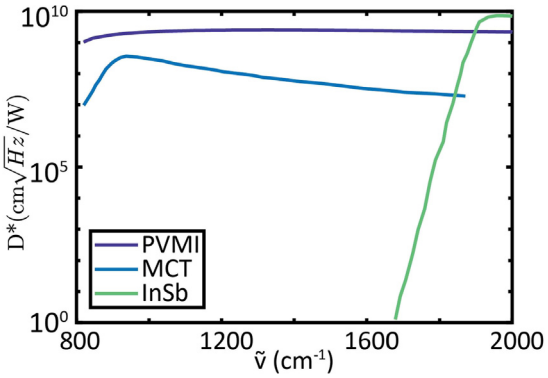

FIGURE 12.2

Normalized detectivity (D^*) comparison for representative IR detectors with three different coatings and configurations. PVMI-MCT detector shows the best spectral responsivity across the entire spectral range compared to conventional MCT detectors. Liquid nitrogen or thermoelectric cooling allows for the best performance and stability.

3.3 Modulating devices

Modulation techniques are common approaches to increase sensitivity for spectroscopic measurements. They can be categorized into modulation of frequency, amplitude, polarization, and wavelength. For frequency modulation, optical heterodyne detection is a general technique to increase SNR by demodulating the desired frequency component out of a noisy background, whereas amplitude modulation is usually integrated to optimize the dynamic range. Polarization modulation, on the other hand, can enhance the structural sensitivity of the imaging system and provide additional chemical information such as molecular-, macromolecular-, and supramolecular-level chirality. Finally, wavelength modulation is achieved not by an external device but also by inducing nonlinear effects in the laser source and by modulating both laser frequency and intensity. This technique is mainly used for detecting samples with narrow linewidth spectral features such as gas-phase samples. In this section, we discuss the working principles and practices of widely used modulating devices such as optical choppers (intensity modulation) and PEM (polarization modulation).

Optical choppers are conventional devices for the intensity modulation of a continuous beam. The chopper blades are controlled by a phase-locked loop motor that maintains the chopping frequency, duty cycle, and phase relative to the reference signal. The intensity is adjusted by tuning the duty cycle and the passing spot size on the blade. While the chopping frequency range can be extended to dual or harmonic frequencies by different blade geometric designs, the maximum chopping frequency is typically limited to 10 kHz. Combination of an optical chopper and an LIA is a typical QCL spectroscopic setup under the continuous wave (CW) mode operation. The advantages include optimizing the SNR improvement by matching the light intensity with the dynamic range of the LIA. Also, the high intensity stability can benefit experiments sensitive to the sample's thermal response [31] when the potential excessive heat transfer from CW is less concerned. Finally, optical choppers allow for a higher duty cycle than that available under the pulsing mode operation, which can facilitate higher efficiency of coupled devices [46].

PEM modulates the light polarization based on the photoelastic effect. The PEM optic comprises an isotropic crystal that changes the refractive index in response to different mechanical strain, such as ZnSe, CaF_2, Si, and fused quartz. Unlike birefrigent materials, where the passing light from different directions is subject to different velocities, PEM is a resonant device. A PEM comprises a piezoelectric transducer that vibrates the optical element by its fundamental resonant frequency, which alters the

applied strain as well as the refractive index periodically. From here, we can infer that the refractive index (n) becomes a time-dependent parameter. Moreover, since the optics is only compressed/stretched along one axis, it leads to a phase difference, or retardation (δ), as a function of time.

$$\delta(t) = z\big(n_x(t) - n_y(t)\big) \tag{12.5}$$

where z denotes the optic thickness, and n_x and n_y stand for the refractive index of two perpendicular optic axes, respectively. A PEM controller applies the oscillation driving force according to the preset incident light wavelength ($n = 2\pi/\lambda$) and desired retardation modulation range, which is usually in the unit of wavelengths. The wide spectral coverage and retardation modulation of PEM enable high-sensitivity polarimetric spectroscopic measurements. The interested modulated polarized component can be encoded in the PEM's resonance frequency and extracted out with an incorporated filtering scheme (Section 4).

3.4 Performance characterization

As with any other imaging modality, the performance metric of a QCL-based spectroscopic imager relies on SNR, imaging speed, and resolution. We usually evaluate the spectral and image quality from the perspective of an imaging system. Nevertheless, depending on applications, additional meticulous characterizations can be required to maintain the experimental precision. For instance, for long-term measurements, temporal noise becomes a major concern, which can stem from the thermal drift, stage motion, and the pulse fluctuations. Unlike thermal sources, QCLs are composed of multiple laser chips that can lead to varying spectral noise and discontinuities at the chip transition regions. Furthermore, acquisition time can be individually changed for each of the spectral bands allowing band-specific SNR enhancement that is not achievable in FT-IR. Lastly, QCLs have some unique characteristics such as pulse-to-pulse noise and polarization that is highly wavenumber- or laser chip-dependent. While theoretically QCL output emissions are typically purely linearly polarized, the residual birefrigent behavior observed in practice can result in additional noise considerations for highly sensitive polarimetric experiments. In this section, we describe characterization methods for the optical spectroscopy/imaging system that includes SNR, laser source polarization, and a conventional approach to gauge the spatial resolution.

Noise affects the detection capability of any spectroscopic imaging system. Noise contributions can occur at various stages in an optical system, and they have been explicitly covered in Ref. [45]. Here, we focus specifically on the laser source considering its noise contributions that dominates the system's performance. A major noise source in QCLs that is absent in FT-IR systems is the pulse-to-pulse fluctuation of the emitted light intensity, and it is highly wavenumber-dependent. For instance, the SNR of a pulse train containing a sufficient number of pulses is evaluated using the AUCs of every single pulse. The voltage profile for a single pulse at four different wavenumbers is displayed in Fig. 12.3. For AUC calculations, a time integral of the whole pulse starting from the baseline voltage is calculated. The standard deviation of the calculated AUCs then gives an estimation of the expected pulse-to-pulse noise. Using a log-ratio plot of coadded pulses and the standard deviation as shown in Fig. 12.3, it is possible to investigate the influence of time-variant noise. Ideally, the time-variant noise is zero, which is reflected by a slope of -0.5 in the log-ratio plot. In this case, there is no time-variant (trend) component responsible for the AUC variations. However, in reality, it is not likely to achieve perfect long-term stability, and the slope is typically larger than -0.5.

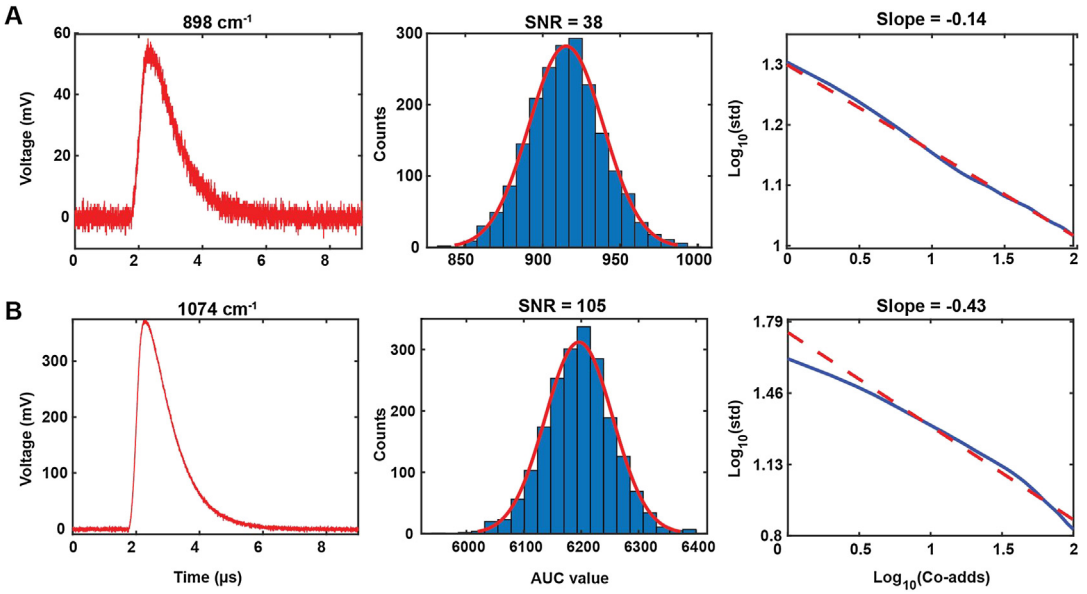

FIGURE 12.3

Laser output characterization using area under the pulse curve (AUC). An example of a single 100 kHz pulse is shown in the first column. The laser output is analyzed through AUC histograms each containing a total of 2000 pulses as shown in the center column. SNR is defined as the ratio of the average AUC divided by the standard deviation (SNR = mean(AUC)/std(AUC)). The laser noise is characterized by the log-ratio of coadd number and standard deviation of AUC, as shown in the third column. A slope close to −0.5 represents white noise characteristics while the deviation suggests time-variant noise characteristics. Four representative laser outputs are demonstrated by the central wavenumber of two of the laser chips: (A) 898 cm^{-1} (B) 1074 cm^{-1}.

Another aspect that needs to be considered for spectroscopic imaging systems is the spectral noise variation. Similar to FT-IR systems, 100% line can be used to evaluate the spectral noise of QCL-based spectroscopy and imaging systems. It is based on the deviation from the total transmission acquired by the two consecutive background measurements. Following the absorbance unit conversion, it is defined as:

$$100\%\text{line} = -\log_{10}\frac{I_{bkg1}}{I_{bkg2}} \tag{12.6}$$

where I_{bkg} is denoted as the light intensity measured at the background (or without any sample). In addition to the distinct laser noise characteristics, 100% line reveals the noise distribution across the spectrum that is dependent on both the laser and the detector's wavenumber-dependent response, system optical alignment, and chromatic aberrations.

Spatial resolution and image contrast are two associated factors contributing to the image quality. To isolate the impact of a sample's chemical contrast from system resolving power, it is conventional to use resolution test targets to evaluate the spatial resolution. One standard sample is USAF 1951

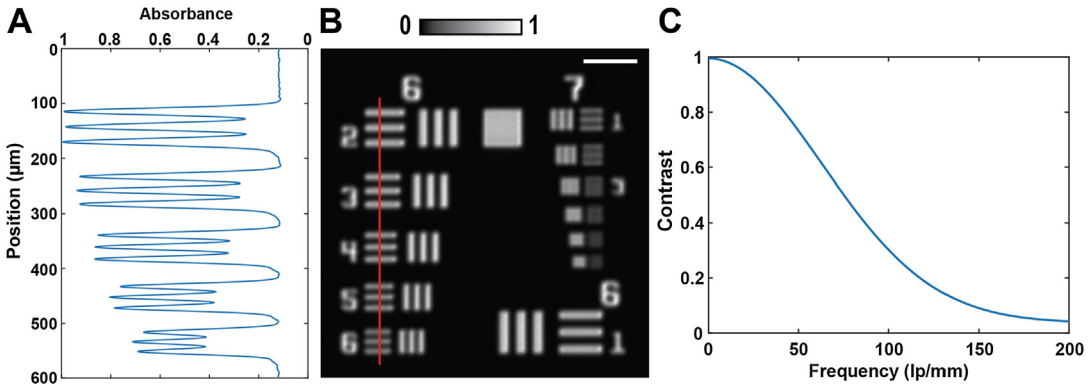

FIGURE 12.4

System spatial resolution characterization using USAF 1951 target (A) Vertical line profile of group 6 denoted as a *red line* in (B) Absorbance image at 1200 cm^{-1}, and the corresponding modulation transfer function (MTF) is shown in (C). Scale bar is 50 μm.

target, which is composed of SU-8 polymer grating patterns with a fixed width but various spacing (periods) as shown in Fig. 12.4A–B. For transmission mode, the substrate is constrained to IR-transparent material such as BaF_2. The polymer patterns provide a strong absorption signal that is ideal for spatial resolution characterization.

Modulation transfer function (MTF) quantifies the contrast transfer efficiency of a linear shift-invariant system. Transfer efficiency is defined by the ratio between the image and object contrast, where the norm (metric 1) suggests that the object contrast is fully recovered in the image. Mathematically, MTF is defined by:

$$\mathrm{MTF}(k) = \frac{|H(k)|}{H(0)} \tag{12.7}$$

where $|H(k)|$ is the modulus of system impulse response as a function of spatial frequency k, and $H(0)$ is the normalization term. Intuitively, higher spatial frequency requires higher resolving power to retain the object contrast (Fig. 12.4C). To calculate the MTF, one approach is to acquire the edge-response of the system. After integrating the sharp edge image projection, the derivative can be served as the impulse response along one dimension. Therefore, a complex-valued system transfer function (H) is acquired after applying FT, and MTF is the modulus part normalized by the DC component as indicated in equation 12.7.

4. Data acquisition

The main issues of spectroscopic data acquisition include signal digitization, online and offline processing, and data recording. We now introduce the working principles and practices of widely used demodulating device for data acquisition, namely, the lock-in amplifier (LIA). LIA is based on the heterodyne detection method which mixes the input signal (V) with a sinusoidal wave from a local

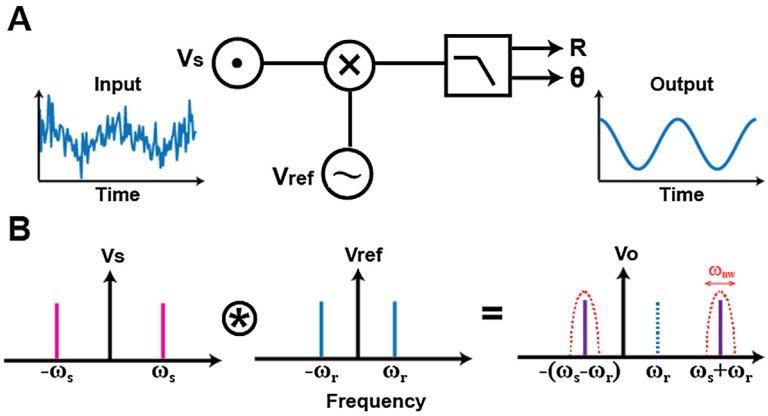

FIGURE 12.5

Working principle of a lock-in amplifier (LIA). (A) Schematic of a typical LIA measurement. A reference signal (V_{ref}) is mixed with an input signal (V_S) and then pass through a low-pass filter. The magnitude (R) and phase (θ) of the interested frequency component within the input signal can be extracted in the output signal (V_o). (B) Sketch of frequency modulation. The time series product results in a convolution operation in the frequency domain, leading to the frequency shift to sum ($\omega_s + \omega_r$) and difference ($\omega_s - \omega_r$) of the input signal frequency (ω_s) and reference signal frequency (ω_r). ω_{BW} is the low-pass filter bandwidth.

oscillator (V_r) to demodulate the desired frequency component (Fig. 12.5A). The output signal (V_o) results in a frequency modulation of the input signal, which can be formulated as:

$$\begin{aligned} V_o(t) &= V_s(t) \times V_r(t) \\ V_s(t) &= \sqrt{2}R\cdot\cos(\omega_s t+\theta) = \frac{R}{\sqrt{2}}e^{+i(\omega_s t+\theta)} + \frac{R}{\sqrt{2}}e^{-i(\omega_s t+\theta)} \\ V_r(t) &= \sqrt{2}e^{i\omega_r t} \\ V_o(t) &= Re^{i((\omega_s+\omega_r)t+\theta)} + Re^{-i((\omega_s-\omega_{sr})t+\theta)} \end{aligned} \tag{12.8}$$

Consider the input signal as a real signal with the desired frequency (ω_s) component embedded, then after mixing with the reference signal (ω_r), the component is frequency-shifted to the sum ($\omega_s + \omega_r$) and difference ($\omega_s - \omega_r$) of the two mixing signal frequencies. The operation is equivalent to a convolution in the frequency domain, as shown in Fig. 12.5B. In practice, the oscillator is usually set to the frequency of interest, i.e., ($\omega_s = \omega_r$) and a low-pass filter (◢) is applied to extract the frequency component such that the extracted output signal $\left(V_o'(t)\right)$ can be expressed in terms of the magnitude (R) and phase (θ):

$$V_o'(t) = \mathscr{L}\{V_o(t)\} = Re^{-i\theta} \tag{12.9}$$

The low pass filter determines the noise filtering effect and should be set according to the input signal characteristics. The filter's response can be described through a frequency-dependent transfer function, $H(\omega)$. Ideally, the low-pass filter only passes input signals with a frequency lower than a

certain cut-off frequency. In practice, however, there exists a transition band between the pass-band and stop-band wherein the input signal is not eliminated but is attenuated. Instead of resorting to the filter's frequency response function, several parameters are usually used to delineate a filter's features. For example, filter bandwidth is defined by the frequency at which the amplitude, $|H(\omega)|$, is attenuated by 3 dB, and the cutoff frequency is the boundary where the signal is entirely filtered. The slope of the transition band is described by the roll-off, which is usually in the units of dB/oct or dB/dec. As indicated in the complex transfer function, a filter also introduces a phase delay, and the slope of the phase shift, $arg\{H(\omega)\}$, determines the output signal's time delay. Conventionally, the time constant (τ) characterizes the time taken for the output signal to become around 0.63 magnitude of its steady state, and the settling time is the period to reach the steady state. While the time constant is defined based on the system's step response in the temporal domain, there exists a direct relation between the time constant (τ) and frequency bandwidth (f_3dB), which can be proved by the fact that pulse response is the derivative of step response:

$$\begin{aligned}
&\text{Step response } U(t) = A\left(1 - e^{-t/\tau}\right) \text{ where } t \geq 0 \\
&\text{Impulse response } \delta(t) = \frac{dU(t)}{d(t)} = \frac{A}{\tau}e^{-t/\tau} \\
&\text{Frequency response } \delta(\omega) = \frac{A}{\tau}\cdot\frac{1}{1/\tau + i\omega} = \frac{A}{1 + i\omega/\omega_0}
\end{aligned} \tag{12.10}$$

where $\omega_0 = 2\pi f_{3dB} = 1/\tau$ denotes the cutoff frequency in radians. It is common to use time constant τ to adjust the bandwidth of LIA's low-pass filter. Common low-pass filters include ButterWorth, Chebyshev, and Elliptic filters, with filter orders defined analytically. While filter type and order should be chosen depending on the input signal, the rule of thumb is that the filter bandwidth needs to cover all of the (electric) signal's significant frequency components. Furthermore, filter roll-off needs to adapt to different acquisition conditions as well. For instance, a higher ADC resolution requires a higher roll-off to differentiate finer amplitude levels. Under a low sampling rate scenario, a higher roll-off is also needed to avoid aliasing. Finally, while a larger time constant (smaller bandwidth) results in a smoother output signal, it leads to a slower response, and vice versa.

5. Applications

We have described some major performance metrics for an IR spectroscopic imaging system. DFIR systems have led to advancements in many different fields spanning from digital histopathology to polymeric detection. In this section, we will mention some of these well-established applications, namely, protein spectroscopy and fast environmental screening of microplastics. We also outline the numerous advantages for tissue imaging ranging from dramatic reduction in imaging time to enabling new information by VCD measurements.

5.1 Protein spectroscopy

Proteins are extremely important biomolecules that are essential for a majority of biological processes. IR spectroscopy is one of the analytical methods that provides structural and quantitative information about proteins in liquid and solid states. These capabilities are leveraged in fields such as biomedical

spectroscopy for tissue and body fluid analysis [47,48], as well as in biotechnology for the study of enzyme activity [49]. QCL light sources have paved the way for highly sensitive protein spectroscopy in aqueous solutions. Compared to thermal emitters such as globars, QCLs can emit much higher light intensities [24]. This increased light intensity is particularly useful for any investigations in the amide I and II regions, where the notoriously strong deformation vibration of H_2O can lead to total absorption even for very small path lengths. By using QCLs, it is possible to drastically increase the path lengths of transmission cells [50]. With QCL spectrometers, path lengths of approximately $\sim$32 µm are common compared to 8 µm for state-of-the-art FT-IR instruments. Alone through the increased path length, the amount of analyte in the cross-section can be increased by a factor of four resulting in an increase in the signal by the same amount. Besides that, the bigger spacing reduces back pressure and clogging of the transmission cells. Taken together, all these advantages enabled by QCL-based spectrometers make it possible to analyze proteins directly in H_2O, which avoids the common substitution of H_2O by D_2O. Combined with the capability of IR spectroscopy to determine and quantify different secondary structure elements based on their amide I and II band shapes [51,52], QCL spectroscopy offers a tool for fast and reliable protein secondary structure analysis in aqueous solutions. The capability to resolve different secondary structures of proteins is displayed in Fig. 12.6, which shows the amide I band of bovine serum albumin (BSA), hemoglobin, α-chymotrypsin, β-lactoglobuline, and lysozyme. The bandshapes are largely influenced by the protein secondary

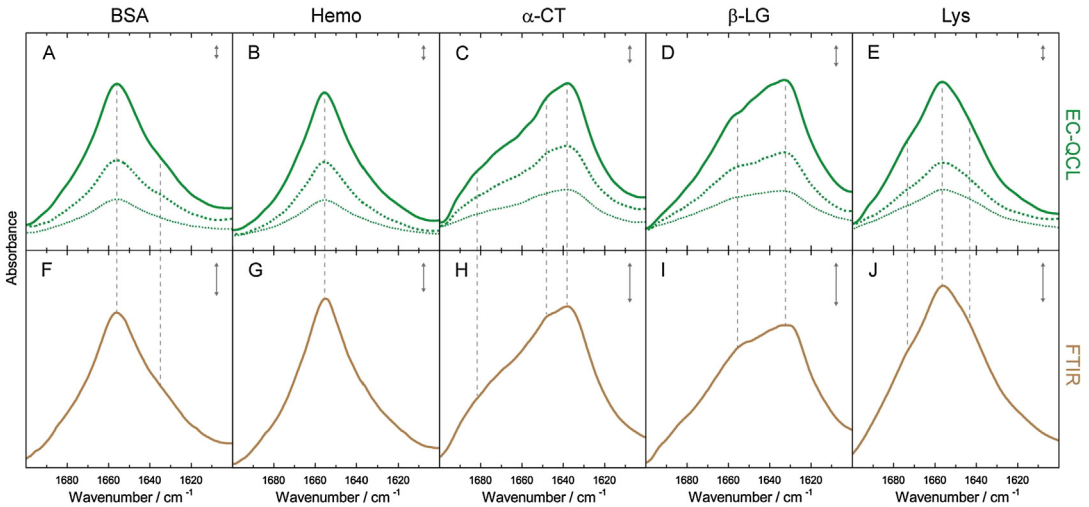

FIGURE 12.6

IR absorbance spectra of 10 mg/mL (*green solid line*), 5 mg/mL (*green dashed line*), and 2.5 mg/mL (*green dotted line*) protein solutions acquired by an EC-QCL setup (A—E) and 20 mg/mL (brown solid line) protein solutions acquired by FT-IR spectroscopy. *Gray dashed lines* highlight the high congruence of the spectral features between the IR spectra acquired by EC-QCL and FT-IR spectroscopy. Gray double-headed *arrows* indicate the absorbance of 10 mAU.

Reprinted (adapted) with permission from Alcaráz et al. [53]. Copyright 2015 American Chemical society. Further permission related to the material excerpted should be directed to the ACS.

structure composition, which is noticeable when comparing BSA and β-lactoglobuline, which are predominately composed of α-helical and β-sheet structures, respectively.

Besides applications in protein characterization [53,54], QCL spectroscopy is useful in the investigation of extremely small concentrations of proteins. It is now possible to detect concentrations as low as 0.0025 mg/mL, an order of magnitude lower than the concentrations that are accessible with the state-of-the-art FT-IR instruments. This was achieved by the integration of balanced detection into QCL-based spectrometers [37].

5.2 Microplastic analysis

IR spectroscopy is well-suited for the analysis of polymers and has been used in this field over decades [55]. The different vibrational modes of polymers provide an excellent description of their chemical structures and allow for the separation of different polymer types. In recent years, polymers in the form of microplastics have become a major environmental concern. With spectroscopic methods, it was possible to detect microplastics even in the most remote areas of the world [56–59]. It has been shown in many studies how these microplastics have an adverse effect on living organisms through their structural and chemical properties [60]. FT-IR and DFIR microspectroscopies are methods that have been successfully applied to the screening of microplastic contaminated samples [61–64]. Besides the pure qualitative characterization of the plastics, microscopy data provide information about the size, shape, and number of plastic particles in the presentative sample. Nevertheless, one of the problems of FT-IR microscopy is the lack of speed for the application to large-scale routine analysis. DFIR imaging allows for a significant speed up in the analysis and is shown to provide equivalent information content to common FT-IR imaging [62,63]. Primpke et al. report a tenfold decrease in imaging time using DFIR imaging, while maintaining comparable levels of confidence in the microplastics detection. Identification and classification of microplastics is an excellent example for an application where highly resolved bandshapes and broad wavenumber availability are not essential to the task. Instead, a high-level of confidence for the classification can be achieved by a simple, statistically viable selection of discrete spectral points. The imaging time is reduced drastically in this way, since it becomes unnecessary to assign regions of interest for the imaging process. Given these promising results, it is expected that DFIR will become a key technique in the broad-scale environmental screening of microplastics.

5.3 Tissue imaging

Tissue imaging is the field where DFIR imaging has found the most applications so far. The potential of IR imaging as a histopathological tool is already well-known for FT-IR based systems [18,65]. Applications within the domain of digital histopathology for IR data cover tissue classification [66,67], digital staining [68], and patient outcome prediction [69,70]. DFIR imaging provides comparable information to FT-IR data with a significant speedup in imaging time. In contrast to FT-IR-based systems, the imaging time for QCL-based DFIR systems is directly proportional to the number of measured discrete spectral data points. Thereby, it is possible to exploit redundancies in the hyperspectral data set for a considerable reduction in imaging time [71–74]. Tiwari et al. [70,75] showed that even for a very reduced number of spectral points, it is still possible to perform an excellent digital staining on IR data. This work highlights how it is possible to accelerate the procedures significantly

without a loss of performance. Fig. 12.7A shows the images of four different colon tissue cores at amide I. The corresponding hematoxylin and eosin (H&E) staining is depicted in Fig. 12.7D.

Besides the applications that are already established by FT-IR imaging and can be enhanced by DFIR imaging, the properties of QCLs allow new applications. QCLs are inherently polarized light sources, which allow the easy integration of VCD imaging capabilities to QCL-based systems [76]. High SNR ratios of the DFIR instruments enable the measurement of minute changes in the response to left- and RCP light. These differences in the absorbance can be attributed to molecular, macromolecular [77,78], and supramolecular [79–81] chirality. Phal et al. [34] showed how it is possible to implement a QCL-based microspectroscopy system that is capable of measuring pixel-wise VCD spectra. Utilizing a PEM, a QCL-based VCD spectroscopic imaging (QCL-VCD) is demonstrated in Ref. [34]. The instrumentation design is shown in Fig. 12.8A. VCD measurements utilize the absorption difference between the right- and LCP light to detect sample's chirality. The QCL laser pulses pass through the 45° polarizer followed by a PEM with the retardance amplitude equal to $\lambda/4$, so that RCP and LCP lights are generated periodically (Fig. 12.8B). After interaction with the sample, the QCL pulses and the resulting VCD signal are demodulated using LIA acquisition scheme as mentioned in Section 4 (Fig. 12.8). As expected, VCD signal is encoded at $f_{qcl} \pm f_{Pem}$, where f_{qcl} is the pulse repetition rate and f_{Pem} is the PEM resonance frequency. Compared with the conventional Fourier Transform VCD (FT-VCD), the band-by-band acquisition scheme of QCL eliminates the need to calibrate the wavelength-dependency. Furthermore, the high throughput of the laser source allows acquiring comparable FT-VCD (typical 30 min to hours) protein spectra with shorter amount of time (2 min) [34]. VCD spectra corresponding to wavenumber 1632 cm^{-1} and 1664 cm^{-1} are displayed in Fig. 12.7B and C, respectively. Both wavenumbers lie within the range of the amide I absorption whereas the absorption at 1632 cm^{-1} can be predominantly attributed to β-sheet secondary structures, the 1632 cm^{-1} band represents primarily the α-helical elements. Detailed information about the instrumental design and the usage of PEMs for polarization are described in earlier sections. The applications for such an instrument are a great tool for scientific applications that aim for a better understanding of chirality in biological processes. In pharmaceutical production, the problem of enantiomeric separation is a critical step in the production process. VCD imaging of powder mixtures for the analysis of enantiomeric purity has the potential to become an important tool in pharmaceutical quality control.

5.4 Phase transition mapping

Ellipsometry is a routinely used technique to measure thickness and dielectric constants of thin films by relating to the optical properties of the material. MIR is an extension of the generalized ellipsometry technique that can be employed for mapping properties of samples arising specifically from polarization. Specific combination of waveplates and polarizers can be used to acquire the polarimetric parameters, for instance, ellipsometric measurements. Spectroscopic MIR ellipsometry can be used to infer not only the sample thickness but also the chemical contrast by acquiring complementary phase and amplitude images concurrently [82,83]. Upon illumination of the polarized light, the light–matter interaction can induce the phase transition and light attenuation, which are closely related to optical properties of the sample. A typical ellipsometry instrumentation (Fig. 12.9) includes a pair of polarizers, where the first one restricts the polarization state of the incident beam, and the second one detects the induced polarization components caused by the sample. Since the second polarizer is typically

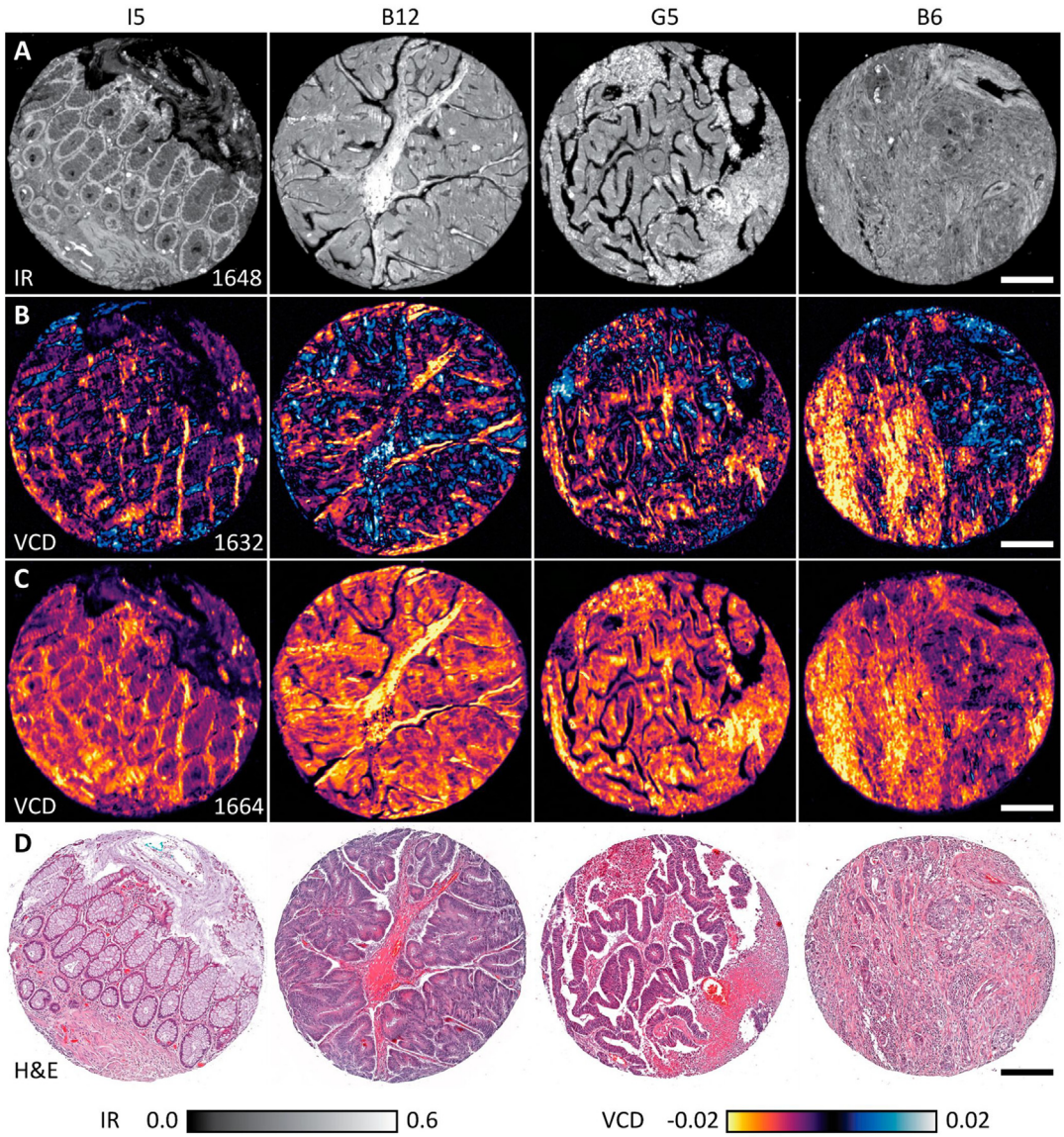

FIGURE 12.7

(A) Infrared amide I (1648 cm^{-1}) absorption, (B) 1632 cm^{-1} VCD, (C) 1664 cm^{-1} VCD, and (D) corresponding H&E-stained images of four samples from a TMA with normal (I5) and various grades of malignant (B12, G5, B6) colon tissue cores. The infrared absorbance and VCD data are acquired in transmission configuration. The alphabetic and numeric identifiers for each core correspond to the row and column of the TMA, respectively. All scale bars are 250 μm.

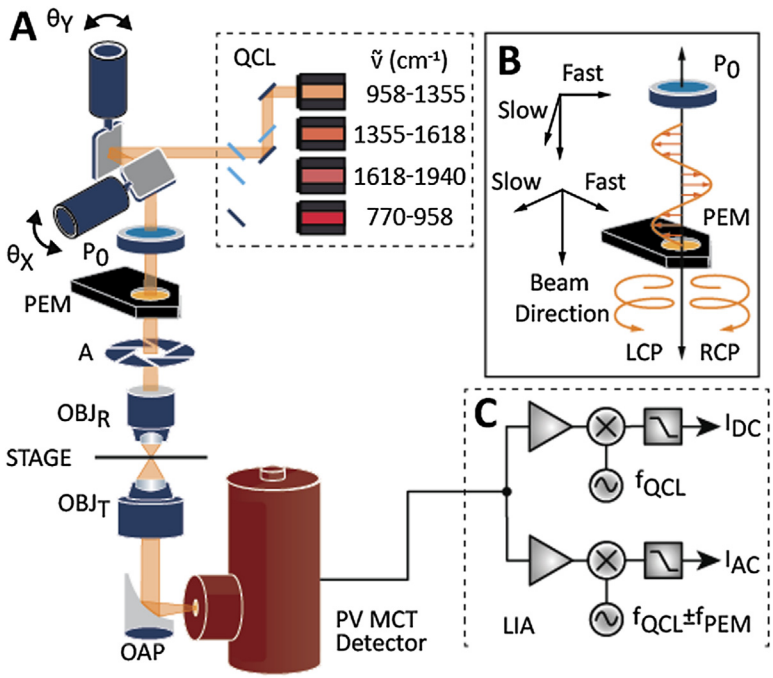

FIGURE 12.8

Vibrational circular dichroism spectroscopic imaging microscope design. (A) Schematic of the point-scanning microscope configuration. QCL pulses repetition frequency (f_{QCL}) is modulated by a PEM (resonance frequency f_{PEM}) and the resulting signal is acquired using a lock-in amplifier (LIA)-based detection scheme. (B) Illustration of circularly polarized light generation through PEM modulation *LCP*, left-circularly polarized light; P_0, 45° polarizer; *RCP*, right-circularly polarized light; *slow/fast*: slow and fast optical axes.

used to examine the sample's optical characteristics, it is called an analyzer. As mentioned in Section 2, polarization states can be formulated with a combination of two different orthogonal components. The electric field vector of any electromagnetic wave, even for an arbitrary polarized light, can be described using a polarization ellipse, denoted by the ellipsometric angles, orientation angle ψ-, and ellipticity Δ. The polarization ellipse is then described by the equation, $\rho = \tan\psi \cdot e^{i\Delta}$.

Ellipsometric measurements can determine both the real and imaginary parts of the complex dielectric function $\overline{\in} = \in_1 + i\in_2$, which directly relates to the complex refractive index, $\overline{n}$, and the attenuation coefficient, k, by the equation $\overline{n} = (n + ik)$. Depending on the sample's structure, the complex refractive index $(\overline{n})$ may vary with polarization states. Therefore, at least four different settings of the polarizer pair are essential for ellipsometry measurements. Using regression analysis on the acquired measurements, ellipsometric parameters including sample thickness, incident wavelength, and complex refractive index can be derived. For example, to evaluate the induced 0° polarization component from incident 90° polarization, the fast axis of the first polarizer is adjusted along

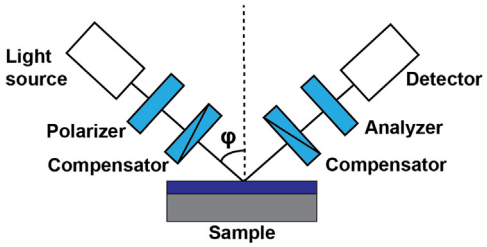

FIGURE 12.9

Schematic of ellipsometry instrumentation with incidence angle ϕ. An ellipsometric measurement optical setup consists of a light source, a polarizer, an analyzer, and compensators, where the polarizer and analyzer synergically interrogate the phase transition induced by the sample. The compensators are optionally used to produce phase retardation to increase data acquisition efficiency.

90° while that of the analyzer is adjusted along 0°, and vice versa for the polarization pair of 45° and 135°. Interested readers are encouraged to refer Ref. [84] for a detailed mathematical derivation. The series of measurements can relate to the ellipsometric angles as follows:

$$\cos 2\psi = \frac{I_{90^\circ} - I_{0^\circ}}{I_{90^\circ} + I_{0^\circ}}$$
$$\sin 2\psi \cos\Delta = \frac{I_{45^\circ} - I_{135^\circ}}{I_{45^\circ} + I_{135^\circ}} \tag{12.11}$$

In general, for anisotropic sample measurements that are highly sensitive, it is advised to acquire phase transition over a large range of incidence angles. Another alternative is to fix the polarizer angle and rotate the analyzer. Incorporation of a PEM (Section 4) or liquid crystals as compensators can modulate the phase and achieve higher efficiency. By determining the complex refractive index, detailed information regarding the structural properties of the sample including morphology and crystallinity can also be mapped. Characteristic vibrational bands such as carbonyl, alkene, and amide can be used to elucidate molecular orientations that pertain to the optical anisotropy, chemical composition, morphology, and film thickness in such samples. Demonstrations spanning phase and amplitude mapping of heterogeneous surfaces to time-resolved temperature-dependent mapping of phase have been shown. It is especially useful for studying thin-film phase transitions [85].

6. Summary

QCL sources have unfolded new opportunities in the field of IR spectroscopy. The fundamental light source difference has led to revolutionary changes in instrumentation design. Contrary to spectral multiplexing resulting from interferometry, the band-by-band based laser pulse emission of QCLs requires a more sophisticated control architecture. This further necessitates unique tailoring for different laser scanning modes and additional devices. With the prior sample's chemical feature information, the high spectral power can enhance the data acquisition efficiency where only significant

spectral bands are acquired while reducing the scanning time. Furthermore, using noise reduction strategies including signal processing and modulation techniques, better trade-off between the scanning speed and SNR can be achieved by the recent advancements in computational power. The speed advantage also allows for more complicated algorithms feasible in real time and broadens the potential applications such as in a clinical setting.

Equipped with these unique properties, QCLs have demonstrated its capabilities in various fields. The high SNR enables a large-scale chemical mapping that is not practical for conventional IR spectroscopy imaging. For example, it benefits environmental studies for microplastic screening and histopathological image analysis on large biological samples such as tissue microarrays. Moreover, the high sensitivity enables better detection limits for common applications such as protein analyses. Additionally, by integrating with polarization modulation devices, QCLs can dramatically reduce the scan time required for weak polarization changes signal such as that from vibrational dichroism. Overall, while the implementation introduces radical changes in instrumentation design and distinct SNR characteristics, QCLs have showcased the capabilities in IR spectroscopy and imaging applications as well as the potential for the advancements of next-generation IR spectroscopic imagers.

7. Future perspectives

IR spectroscopy and microspectroscopy have been constantly pushing the limits in terms of both accuracy and precision of its measurements. The field has seen substantial improvements in the last decades in terms of accuracy, and the pace of innovation in recent years suggests no end of this development in the near future. By far the most defining upheaval of the past years is the broad integration of QCLs into this specific field of spectroscopy. With the rise of the QCL, spectral and spatial accuracy could be brought to a new level. In laser-based spectroscopy, the limiting noise factor at this moment can be attributed to laser instabilities. Balanced detection is one of the technological innovations that allow to mitigate exactly that problem. Another approach relies on the leveraging of the electric field that is emitted by impulsively excited molecular vibrations. Thereby the laser-associated noise can be almost completely eliminated. Similar to photothermal and photoacoustic effects, the evaluation of the electric field is leveraging secondary effects instead of directly evaluating the absorbance signal itself. Increasing interest in the secondary effects of the IR radiation has led to a paradigm shift and is promising to enable new levels of accuracy. This is of particular relevance to the application on biofluids where minute spectral changes can be observed to investigate biomarkers that are predictive of certain health conditions. At this point in time, it is not unlikely that the increase in accuracy will make IR spectroscopy a game changer in shifting the health sector from acute to preventive treatment. A second major implication will be the better understanding of biomolecular interactions. Two major preconditions need to be fulfilled to allow for these types of investigations: high time resolution and high SNR. If both factors are ensured, another application could lie in the evaluation of secondary effects of the IR radiation. Additionally, techniques such as IR-OH promise way faster imaging times that will be extensively beneficial. IR-OH measurements contain a not yet seen information content, extensive compositional and excellent spatial information. With high quality chemical and morphological tissue data, combined with artificially intelligence, this will be the next leap forward.

References

[1] P. Mukherjee, A. Ghosh, N. Spegazzini, M.J. Lamborn, M.M. Monwar, P.J. DesLauriers, R. Bhargava, Relating post-yield mechanical behavior in polyethylenes to spatially varying molecular deformation using infrared spectroscopic imaging: homopolymers, Macromolecules 51 (10) (2018) 3836−3844.

[2] O. Arteaga, Spectroscopic sensing of reflection optical activity in achiral $AgGaS_2$, Opt. Lett. 40 (18) (2015) 4277−4280.

[3] N. Kröger-Lui, N. Gretz, K. Haase, B. Kränzlin, S. Neudecker, A. Pucci, A. Regenscheit, A. Schönhals, W. Petrich, Rapid identification of goblet cells in unstained colon thin sections by means of quantum cascade laser-based infrared microspectroscopy, Analyst (Cambridge, U.K.) 140 (7) (2015) 2086−2092.

[4] S. Mittal, K. Yeh, L.S. Leslie, S. Kenkel, A. Kajdacsy-Balla, R. Bhargava, Simultaneous cancer and tumor microenvironment subtyping using confocal infrared microscopy for all-digital molecular histopathology, Proc. Natl. Acad. Sci. U.S.A. 115 (25) (2018) E5651−E5660.

[5] J.A. Reffner, P.A. Martoglio, G.P. Williams, Fourier transform infrared microscopical analysis with synchrotron radiation: the microscope optics and system performance, Rev. Sci. Instrum. 66 (2) (1995) 1298−1302.

[6] R. Bosch, Focusing infrared edge and synchrotron radiation with a large numerical aperture, Nucl. Instrum. Methods Phys. Res. Sect. A. 492 (1−2) (2002) 284−298.

[7] A.K. Kodali, M. Schulmerich, J. Ip, G. Yen, B.T. Cunningham, R. Bhargava, Narrowband mid-infrared reflectance filters using guided mode resonance, Anal. Chem. 82 (13) (2010) 5697−5706.

[8] J.-N. Liu, M.V. Schulmerich, R. Bhargava, B.T. Cunningham, Optimally designed narrowband guided-mode resonance reflectance filters for mid-infrared spectroscopy, Opt. Express 19 (24) (2011) 24182−24197.

[9] J.-N. Liu, M.V. Schulmerich, R. Bhargava, B.T. Cunningham, Sculpting narrowband fano resonances inherent in the large-area mid-infrared photonic crystal microresonators for spectroscopic imaging, Opt. Express 22 (15) (2014) 18142−18158.

[10] R. Bhargava, I.W. Levin, Time-resolved fourier transform infrared spectroscopic imaging, Appl. Spectrosc. 57 (4) (2003) 357−366.

[11] R. Bhargava, S.-Q. Wang, J.L. Koenig, FT-IR microspectroscopy of polymeric systems, in: Liquid Chromatography/FT-IR Microspectroscopy/Microwave Assisted Synthesis, Springer, 2003, pp. 137−191.

[12] S.G. Kazarian, Perspectives on infrared spectroscopic imaging from cancer diagnostics to process analysis, Spectrochim. Acta Part. A. 251 (2021) 119413.

[13] R. Bhargava, B.G. Wall, J.L. Koenig, Comparison of the FT-IR mapping and imaging techniques applied to polymeric systems, Appl. Spectrosc. 54 (4) (2000) 470−479.

[14] T. Ribar, J.L. Koenig, R. Bhargava, FT-IR imaging of polymer dissolution. 2. Solvent/nonsolvent mixtures, Macromolecules 34 (23) (2001) 8340−8346.

[15] S.G. Kazarian, K.L.A. Chan, "Chemical photography" of drug release, Macromolecules 36 (26) (2003) 9866−9872.

[16] R. Bhargava, I.W. Levin, Noninvasive imaging of molecular dynamics in heterogeneous materials, Macromolecules 36 (1) (2003) 92−96.

[17] C.M. Snively, G. Oskarsdottir, J. Lauterbach, Parallel analysis of the reaction products from combinatorial catalyst libraries, Angew. Chem. Int. Edition 40 (16) (2001) 3028−3030.

[18] D.C. Fernandez, R. Bhargava, S. Hewitt, I. Levin, Infrared spectroscopic imaging for observer-invariant histopathology, Nat. Biotechnol. 23 (2005) 469−474.

[19] M.C. Martin, C. Dabat-Blondeau, M. Unger, J. Sedlmair, D.Y. Parkinson, H.A. Bechtel, B. Illman, J.M. Castro, M. Keiluweit, D. Buschke, et al., 3D spectral imaging with synchrotron fourier transform infrared spectro-microtomography, Nat. Methods 10 (9) (2013) 861−864.

[20] R. Reddy, D. Mayerich, M. Walsh, M. Schulmerich, P.S. Carney, R. Bhargava, Optimizing the design of FT-IR spectroscopic imaging instruments to obtain increased spatial resolution of chemical species, in: 2012 9th IEEE International Symposium on Biomedical Imaging (ISBI), IEEE, 2012, pp. 354−357.

[21] K.L.A. Chan, S.G. Kazarian, Aberration-free FT-IR spectroscopic imaging of live cells in microfluidic devices, Analyst (Cambridge, U.K.) 138 (14) (2013) 4040−4047.
[22] S.G. Kazarian, K.L.A. Chan, ATR FT-IR spectroscopic imaging: recent advances and applications to biological systems, Analyst (Cambridge, U.K.) 138 (7) (2013) 1940−1951.
[23] M. Kastyak-Ibrahim, M. Nasse, M. Rak, C. Hirschmugl, M. Del Bigio, B. Albensi, K.M. Gough, Biochemical label-free tissue imaging with subcellular-resolution synchrotron FT-IR with focal plane array detector, Neuroimage 60 (1) (2012) 376−383.
[24] J. Faist, F. Capasso, D.L. Sivco, C. Sirtori, A.L. Hutchinson, A.Y. Cho, Quantum cascade laser, Science 264 (5158) (1994) 553−556.
[25] B.G. Lee, M.A. Belkin, R. Audet, J. MacArthur, L. Diehl, C. Pflügl, F. Capasso, D.C. Oakley, D. Chapman, A. Napoleone, et al., Widely tunable single-mode quantum cascade laser source for mid-infrared spectroscopy, Appl. Phys. Lett. 91 (23) (2007) 231101.
[26] Y. Yao, A.J. Hoffman, C.F. Gmachl, Mid-infrared quantum cascade lasers, Nat. Photon. 6 (7) (2012) 432−439.
[27] R. Bhargava, Infrared spectroscopic imaging: the next generation, Appl. Spectrosc. 66 (10) (2012) 1091−1120.
[28] H.-J. Butt, B. Cappella, M. Kappl, Force measurements with the atomic force microscope: technique, interpretation and applications, Surf. Sci. Rep. 59 (1−6) (2005) 1−152.
[29] A. Dazzi, F. Glotin, R. Carminati, Theory of infrared nanospectroscopy by photothermal induced resonance, J. Appl. Phys. 107 (12) (2010) 124519.
[30] S. Kenkel, S. Mittal, R. Bhargava, Closed-loop atomic force microscopy-infrared spectroscopic imaging for nanoscale molecular characterization, Nat. Commun. 11 (1) (2020) 1−10.
[31] M. Schnell, S. Mittal, K. Falahkheirkhah, A. Mittal, K. Yeh, S. Kenkel, A. Kajdacsy-Balla, P.S. Carney, R. Bhargava, All-digital histopathology by infrared-optical hybrid microscopy, Proc. Natl. Acad. Sci. U.S.A. 117 (7) (2020) 3388−3396.
[32] Y. Phal, K. Yeh, R. Bhargava, Polarimetric infrared spectroscopic imaging using quantum cascade lasers, in: J.-X. Cheng, W. Min, G.J. Simpson (Eds.), Advanced Chemical Microscopy for Life Science and Translational Medicine, vol. 11252, International Society for Optics and Photonics, SPIE, 2020, pp. 36−45.
[33] P. Koziol, D. Liberda, W.M. Kwiatek, T.P. Wrobel, Macromolecular orientation in biological tissues using a four- polarization method in FT-IR imaging, Anal. Chem. 92 (19) (2020) 13313−13318.
[34] Y. Phal, K. Yeh, R. Bhargava, Concurrent vibrational circular dichroism measurements with infrared spectroscopic imaging, Anal. Chem. 93 (3) (2021) 1294−1303.
[35] Y. Phal, K. Yeh, R. Bhargava, Discrete frequency infrared vibrational circular dichroism spectroscopy & imaging, in: Novel Techniques in Microscopy, Optical Society of America Technical Digest Biophotonics Congress, 2021 pp. NW3C−1.
[36] Y. Phal, K. Yeh, R. Bhargava, Mid-IR laser-based polarimetric imaging for polymeric and biological applications, in: Advanced Chemical Microscopy for Life Science and Translational Medicine 2021, vol. 11656, International Society for Optics and Photonics, 2021, p. 1165619.
[37] C.K. Akhgar, G. Ramer, M. Zbik, A. Trajnerowicz, J. Pawluczyk, A. Schwaighofer, B. Lendl, The next generation of IR spectroscopy: EC-QCL-based mid-IR transmission spectroscopy of proteins with balanced detection, Anal. Chem. 92 (14) (2020) 9901−9907.
[38] Y. Phal, L. Pfister, P.S. Carney, R. Bhargava, Resolution limit in infrared chemical imaging, J. Phys. Chem. C 126 (23) (2022) 9777−9783, https://doi.org/10.1021/acs.jpcc.2c00740.
[39] L. Lux, Y. Phal, P.-H. Hsieh, R. Bhargava, On the limit of detection in infrared spectroscopic imaging, Appl. Spectrosc. 76 (1) (2022) 105−117.
[40] D.H. Goldstein, Polarized Light, Revised and Expanded, CRC Press, 2003. Ch. 3/5.
[41] P. Janassek, S. Hartmann, A. Molitor, F. Michel, W. Elsäßer, Investigations of the polarization behavior of quantum cascade lasers by Stokes parameters, Opt. Lett. 41 (2) (2016) 305−308.
[42] W.-L. Hsu, J. Davis, K. Balakrishnan, M. Ibn-Elhaj, S. Kroto, N. Brock, S. Pau, Polarization microscope using a near infrared full-Stokes imaging polarimeter, Opt. Express 23 (2015) 4357−4368.

[43] P.K. Barman, P.V. Sarma, M.M. Shaijumon, R.N. Kini, High degree of circular polarization inWS_2 Spiral nanostructures induced by broken symmetry, Sci. Rep. 9 (2019) 1−7.
[44] A. Rogalski, Infrared detectors: status and trends, Prog. Quant. Electron. 27 (2−3) (2003) 59−210.
[45] Y. Phal, K. Yeh, R. Bhargava, Design considerations for discrete frequency infrared microscopy systems, Appl. Spectrosc. 75 (9) (2021) 1067−1092.
[46] H. Sato, M. Shimizu, K. Watanabe, J. Yoshida, I. Kawamura, J. Koshoubu, Multidimensional vibrational circular dichroism apparatus equipped with quantum cascade laser and its use for investigating some peptide systems containing D-amino acids, Anal. Chem. 93 (5) (2021) 2742−2748.
[47] C. Hughes, G. Clemens, B. Bird, T. Dawson, K.M. Ashton, M.D. Jenkinson, A. Brodbelt, M. Weida, E. Fotheringham, M. Barre, et al., Introducing discrete frequency infrared technology for high-throughput biofluid screening, Sci. Rep. 6 (1) (2016) 1−8.
[48] M. Brandstetter, B. Lendl, Tunable mid-infrared lasers in physical chemosensors towards the detection of physiologically relevant parameters in biofluids, Sens. Actuators B 170 (2012) 189−195.
[49] A. Schwaighofer, C.K. Akhgar, B. Lendl, Broadband laser-based mid-IR spectroscopy for analysis of proteins and monitoring of enzyme activity, Spectrochim. Acta Part. A. 253 (2021) 119563.
[50] A. Schwaighofer, M. Montemurro, S. Freitag, C. Kristament, M.J. Culzoni, B. Lendl, Beyond fourier transform infrared spectroscopy: external cavity quantum cascade laser-based mid-infrared transmission spectroscopy of proteins in the amide I and amide II region, Anal. Chem. 90 (11) (2018) 7072−7079.
[51] D.M. Byler, H. Susi, Examination of the secondary structure of proteins by deconvolved FT-IR spectra, Biopolymers Orig. Res. Biomol. 25 (3) (1986) 469−487.
[52] J. Kong, S. Yu, Fourier transform infrared spectroscopic analysis of protein secondary structures, Acta Biochim. Biophys. Sin. 39 (8) (2007) 549−559.
[53] M.R. Alcaraz, A. Schwaighofer, C. Kristament, G. Ramer, M. Brandstetter, H. Goicoechea, B. Lendl, External-cavity quantum cascade laser spectroscopy for mid-IR transmission measurements of proteins in aqueous solution, Anal. Chem. 87 (13) (2015) 6980−6987.
[54] A. Schwaighofer, M.R. Alcaraz, L. Lux, B. Lendl, pH titration of β-Lactoglobulin monitored by laser-based mid-IR transmission spectroscopy coupled to chemometric analysis, Spectrochim. Acta Part. A. 226 (2020) 117636.
[55] K. Holland-Moritz, H.W. Siesler, Infrared spectroscopy of polymers, Appl. Spectrosc. Rev. 11 (1) (1976) 1−55.
[56] L.D.K. Kanhai, K. Gardfeldt, T. Krumpen, R.C. Thompson, I. O'Connor, Microplastics in sea ice and seawater beneath IceFloes from the arctic ocean, Sci. Rep. 10 (1) (2020) 1−11.
[57] G. Suaria, V. Perold, J.R. Lee, F. Lebouard, S. Aliani, P.G. Ryan, Floating macro-and microplastics around the southern ocean: results from the antarctic circumnavigation expedition, Environ. Int. 136 (2020) 105494.
[58] M. Bergmann, S. Mützel, S. Primpke, M.B. Tekman, J. Trachsel, G. Gerdts, White and wonderful? microplastics prevail in snow from the alps to the arctic, Sci. Adv. 5 (8) (2019) eaax1157.
[59] S. Allen, D. Allen, V.R. Phoenix, G. Le Roux, P.D. Jiménez, A. Simonneau, S. Binet, D. Galop, Atmospheric transport and deposition of microplastics in a remote mountain catchment, Nat. Geosci. 12 (5) (2019) 339−344.
[60] T. Kögel, Ø. Bjorøy, B. Toto, A.M. Bienfait, M. Sanden, Micro-and nanoplastic toxicity on aquatic life: determining factors, Sci. Total Environ. 709 (2020) 136050.
[61] A.S. Tagg, M. Sapp, J.P. Harrison, J.J. Ojeda, Identification and quantification of microplastics in wastewater using focal plane array-based reflectance micro-FT-IR imaging, Anal. Chem. 87 (12) (2015) 6032−6040.
[62] S. Primpke, M. Godejohann, G. Gerdts, Rapid identification and quantification of microplastics in the environment byQCL-based hyperspectral infrared chemical imaging, Environ. Sci. Technol. 54 (24) (2020) 15893−15903.
[63] S. Primpke, M. Godejohann, J. Rowlette, G. Gerdts, High-throughput environmental microplastic identification and quantification using a wide-field QCL-IR based microscope, in: Optical Fibers and Sensors for Medical Diagnostics, Treatment and Environmental Applications XXI, vol. 11635, International Society for Optics and Photonics, 2021, p. 1163512.

[64] J.-L. Xu, K.V. Thomas, Z. Luo, A.A. Gowen, FTIR and Raman imaging for microplastics analysis: state of the art, challenges and prospects, Trac. Trends Anal. Chem. 119 (2019) 115629.
[65] R. Bhargava, Towards a practical fourier transform infrared chemical imaging protocol for cancer histopathology, Anal. Bioanal. Chem. 389 (4) (2007) 1155−1169.
[66] M.J. Baker, E. Gazi, M.D. Brown, J.H. Shanks, N.W. Clarke, P. Gardner, Investigating FT-IR based histopathology for the diagnosis of prostate cancer, J. Biophot. 2 (1−2) (2009) 104−113.
[67] F. Großerueschkamp, A. Kallenbach-Thieltges, T. Behrens, T. Brüning, M. Altmayer, G. Stamatis, D. Theegarten, K. Gerwert, Marker-free automated histopathological annotation of lung tumour subtypes by FT-IR imaging, Analyst (Cambridge, U.K.) 140 (7) (2015) 2114−2120.
[68] D. Mayerich, M.J. Walsh, A. Kadjacsy-Balla, P.S. Ray, S.M. Hewitt, R. Bhargava, Stain-less staining for computed histopathology, Technology 3 (01) (2015) 27−31.
[69] J.T. Kwak, A. Kajdacsy-Balla, V. Macias, M. Walsh, S. Sinha, R. Bhargava, Improving prediction of prostate cancer recurrence using chemical imaging, Sci. Rep. 5 (1) (2015) 1−10.
[70] S. Tiwari, A. Kajdacsy-Balla, J. Whiteley, G. Cheng, S.M. Hewitt, R. Bhargava, INFORM: INFrared-based organizational measurements of tumor and its microenvironment to predict patient survival, Sci. Adv. 7 (6) (2021) eabb8292.
[71] K. Yeh, S. Kenkel, J.-N. Liu, R. Bhargava, Fast infrared chemical imaging with a quantum cascade laser, Anal. Chem. 87 (1) (2014) 485−493.
[72] K. Yeh, D. Lee, R. Bhargava, Multicolor discrete frequency infrared spectroscopic imaging, Anal. Chem. 91 (3) (2019) 2177−2185.
[73] P. Bassan, M.J. Weida, J. Rowlette, P. Gardner, Large scale infrared imaging of tissue micro arrays (TMAs) using a tunable quantum cascade laser (QCL) based microscope, Analyst (Cambridge, U.K.) 139 (16) (2014) 3856−3859.
[74] C. Kuepper, A. Kallenbach-Thieltges, H. Juette, A. Tannapfel, F. Großerueschkamp, K. Gerwert, QCL-based infrared microscopy for label-free and automated cancer classification in tissue sections, Sci. Rep. 8 (1) (2018) 7717.
[75] S. Tiwari, J. Raman, V. Reddy, A. Ghetler, R.P. Tella, Y. Han, C.R. Moon, C.D. Hoke, R. Bhargava, Towards translation of discrete frequency infrared spectroscopic imaging for digital histopathology of clinical biopsy samples, Anal. Chem. 88 (20) (2016) 10183−10190.
[76] S. Ludeke, M. Pfeifer, P. Fischer, Quantum-cascade laser-based vibrational circular dichroism, J. Am. Chem. Soc. 133 (15) (2011) 5704−5707.
[77] Y. Phal, K. Yeh, R. Bhargava, Chirality mapping in microscopy format, Optics Photonics News 32 (2021) 12.
[78] V. Baumruk, T.A. Keiderling, Vibrational circular dichroism of proteins in water solution, J. Am. Chem. Soc. 115 (15) (1993) 6939−6942.
[79] D. Kurouski, R.K. Dukor, X. Lu, L.A. Nafie, I.K. Lednev, Normal and reversed supramolecular chirality of insulin fibrils probed by vibrational circular dichroism at the protofilament level of fibril structure, Biophys. J. 103 (3) (2012) 522−531.
[80] D. Kurouski, J.D. Handen, R.K. Dukor, L.A. Nafie, I.K. Lednev, Supramolecular chirality in peptide microcrystals, Chem. Commun. 51 (1) (2014) 89−92.
[81] H. Sato, T. Yajima, A. Yamagishi, Chiroptical studies on supramolecular chirality of molecular aggregates, Chirality 27 (10) (2015) 659−666.
[82] J. Qi, D.S. Elson, A high definition mueller polarimetric endoscope for tissue characterisation, Sci. Rep. 6 (1) (2016) 1−11.
[83] K. Hinrichs, T. Shaykhutdinov, C. Kratz, A. Furchner, Brilliant mid-infrared ellipsometry and polarimetry of thin films: toward laboratory applications with laser based techniques, J. Vac. Sci. Technol. B, Nanotechnol. & Microelectr. Mater. Process. Measur. & Phenom. 37 (6) (2019) 060801.
[84] M. Schubert, Theory and application of generalized ellipsometry, in: H.G. Tompkins, E.A. Irene (Eds.), Handbook of Ellipsometry, William Andrew Publishing, Norwich, NY, 2005, pp. 637−717.
[85] K. Hinrichs, C. Kratz, A. Furchner, Hyperspectral mid-infrared ellipsometric measurements in the twinkling of an eye, Spectrosc. Europe (2020).